Science Advances
AAAS

Supplementary Materials for

Disordered-nanoparticle–based etalon for ultrafast humidity-responsive colorimetric sensors and anti-counterfeiting displays

Chunghwan Jung, Soo-Jung Kim, Jaehyuck Jang, Joo Hwan Ko, Doa Kim, Byoungsu Ko, Young Min Song, Sung-Hoon Hong*, Junsuk Rho*

*Corresponding author. Email: shong@etri.re.kr (S.-H.H.); jsrho@postech.ac.kr (J.R.)

Published 11 March 2022, *Sci. Adv.* **8**, eabm8598 (2022)
DOI: 10.1126/sciadv.abm8598

The PDF file includes:

Other Supplementary Material for this manuscript includes the following:

Supplementary Text 1: Comparison of optical structures: HM, MNHM, and MHM

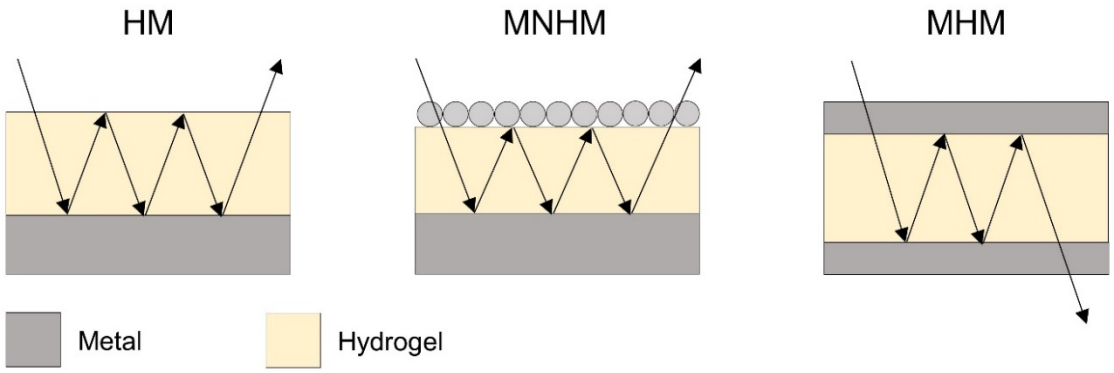

Figure. S1 Comparison with multi-layered interferometers for colorimetric sensors.

Multi-layered interferometers, *i.e.* hydrogel-metal (HM) *(16, 19, 20)* and metal-hydrogel-metal (MHM) *(23)* structures, are widely used for optical sensors because those structures are not only generating vivid colors through interference phenomena, but also have advantages in low fabrication prices, easy manufacturing, and the possibility of large-area processing. These structures are used as colorimetric sensors by adopting an active hydrogel layer because the reflection/transmission spectrum reacts sensitively according to the change of refractive index and thickness of the hydrogel with respect to the stimuli. Despite their distinctive features, the HM and MHM structures are difficult to achieve high color purity and fast response speed at the same time. In HM structure, the hydrogel layer is exposed to the surrounding, which ensures fast response/recovery against the change of surrounding condition. However, the resonance of HM structure relies on Fresnel reflection of a single layer, thus implying low-Q resonance and low color purity. In MHM configuration, the metal layers sandwiching the active medium hinders gas penetration so the response and recovery time is quite slow. On the other hand, the Fabry-Pérot resonance allows the light at the specific wavelengths to be transmitted so that a relatively high-Q spectrum can be obtained.

The proposed metal nanoparticle-hydrogel-metal (MNHM) has utilized disordered metal nanoparticles as the upper layer. Disordered plasmonic structures composed of nanoparticles that are much smaller than the wavelength can be manufactured inexpensively *(32)*, unlike periodic plasmonic metasurfaces, and work effectively like a highly-absorbing dielectric material to achieve high color purity in the reflection spectrum *(28, 31)*. Additionally, the MNHM shows

ultrafast response time coming close to the bare hydrogel because mesoporous disordered structure hardly hinders the penetration of gas molecules. Thus, we can expect both color purity and fast response time in MNHM structure.

Table. S1. Comparison of the characteristics in various optical structures: HM, MNHM, and MHM

Type	HM	MNHM	MHM
Layered structure	Hydrogel- Metal	Metal nanoparticle-Hydrogel-Metal	Metal-Hydrogel-Metal
Color purity	Low	High	High
sRGB area	< 60%	~ 90%	> 90%
Response time	Very fast	Very fast	Slow
Device type	Reflection	Reflection	Transmission

Supplementary Text 2: Calculation of effective refractive index using S-parameter retrieval method

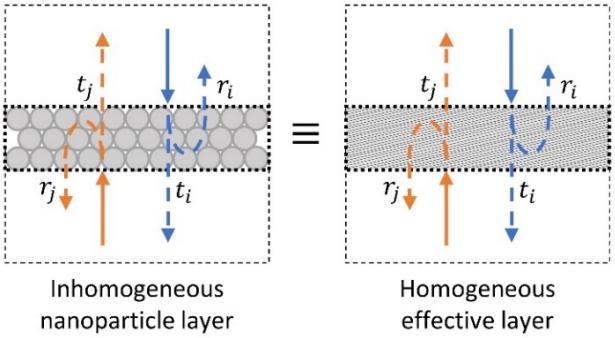

Figure. S2. Schematic of effective layer analysis using S-parameter retrieval.

When the size of nanoparticles that consists of a layer is comparable to the subwavelength scale, the layer can be considered as an effective medium with the effective refractive indices, *i.e.* effective medium theory (Fig. S2) *(39)*. The optical properties of the effective medium can be calculated using the S-parameter retrieval method that allows the extraction of the effective refractive indices with the reflection/transmission coefficient of the original layer *(40)*. In general, the relationship between optical parameters is described as following equation *(39)*,

$$\epsilon = \frac{n}{Z} \; and \; \mu = nZ \tag{S2-1}$$

, where ϵ, n, Z, and μ are permittivity, refractive index, impedance, and permeability of the layer, respectively. For symmetrical layers, the reflection/transmission coefficients r_{ji} and t_{ij} are as follows

$$r_{ji} = r_{ij} = \frac{1}{\cos(nkd) - \frac{\hat{j}}{2}(Z + \frac{1}{Z})\sin(Zkd)}, \tag{S2-2}$$

$$t_{ij} = t_{ji} = \frac{\hat{j}}{2}\left(\frac{1}{Z} - Z\right)\sin(nkd), \tag{S2-3}$$

where k, Z, and d are wavevector, wave impedance, and thickness of the inhomogeneous layer. As a result, the effective refractive index can be calculated as

$$n = \frac{1}{kd}\cos^{-1}\left[\frac{1 - t_{ij}t_{ji} + r_{ij}^2}{2r_{ij}}\right]. \tag{S2-4}$$

Supplementary Text 3: Analytic approach to calculate reflectance of MNHM etalon with scattering matrix modeling

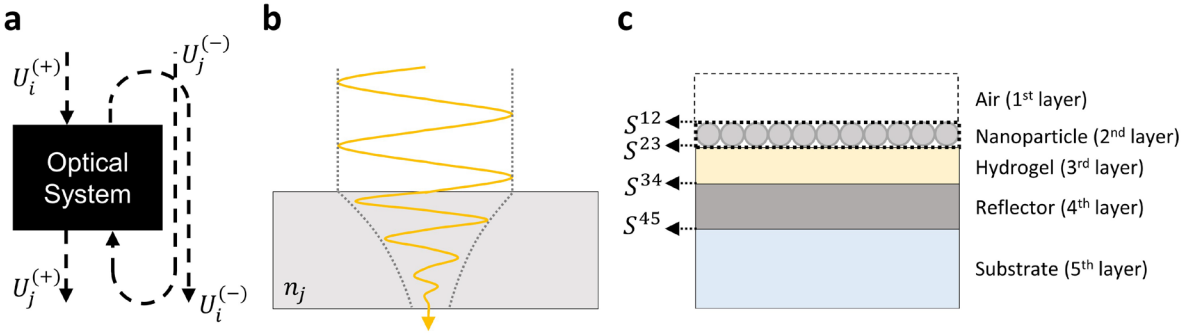

Figure. S3. Calculation of the reflectance of MNHM structure using scattering matrix. (a) Schematics of the defined optical system for scattering matrix. (b) Electrical field attenuation during the propagation in the j^{th} layer. (c) Schematic of MNHM structure with scattering matrices of each interface.

Analysis of multilayered structures could be conducted using a scattering matrix *(29)*. The scattering matrix represents the relationship of the waves toward forward and backward in the optical system (Fig. S3a). In this system, the incoming and outgoing wave, $U_{i,j}^{(\pm)}$, are expressed as scattering matrix, S^{ij}, whose elements are the reflection/transmission coefficients, r and t (Eq. S3-1).

$$\begin{bmatrix} U_j^{(+)} \\ U_i^{(-)} \end{bmatrix} = \begin{bmatrix} t_{ij} & r_{ji} \\ r_{ij} & t_{ji} \end{bmatrix} \begin{bmatrix} U_i^{(+)} \\ U_j^{(-)} \end{bmatrix} = S^{ij} \begin{bmatrix} U_i^{(+)} \\ U_j^{(-)} \end{bmatrix}. \quad \text{(S3-1)}$$

In the case of the normal incidence, the scattering matrix, composed of the reflection and transmission coefficients, can be acquired by the following equation:

$$S^{ij} = \begin{bmatrix} t_{ij} & r_{ji} \\ r_{ij} & t_{ji} \end{bmatrix} = \frac{1}{n_i + n_j} \begin{bmatrix} 2n_i & n_j - n_i \\ n_i - n_j & 2n_j \end{bmatrix} \quad \text{(S3-2)}$$

, where the n represents the complex refractive index of the layer. The real part of the refractive index is used to get the phase retardation, and the imaginary part is used to obtain the attenuation factor, α, of the wave propagating in the layer (Fig. S3b). The relationship between the refractive index and attenuation factor is shown in the following equation,

$$n_j = \Re(n_j) + \hat{\imath}\,\Im(n_j) = \Re(n_j) + \hat{\imath}\frac{\alpha_j}{2k_0} \quad \text{(S3-3)}$$

, where k_0 is the wavevector at the free space. Unlike the conventional lossless system ($\alpha = 0$), one must consider the wave attenuation because the high absorption could occur in the lossy nanoparticle layer. Scattering matrices in a layered structure are calculated in order with the Redheffer star product relation. The generalized Redheffer star product relation is expressed as

$$S^{ik} = S^{ij} * S^{jk} = \begin{bmatrix} t_{ik} & r_{ki} \\ r_{ik} & t_{ki} \end{bmatrix} = \begin{bmatrix} \dfrac{t_{ij}t_{jk}P_j}{1 - r_{ji}r_{jk}P_j^2} & r_{kj} + \dfrac{t_{kj}t_{jk}r_{ji}P_j^2}{1 - r_{jk}r_{ji}P_j^2} \\ r_{ij} + \dfrac{t_{ij}t_{ji}r_{jk}P_j^2}{1 - r_{ji}r_{jk}P_j^2} & \dfrac{t_{kj}t_{ji}P_j}{1 - r_{jk}r_{ji}P_j^2} \end{bmatrix}, \quad \text{(S3-4)}$$

$$where\ P_j = \exp\left(-\left(\frac{\alpha_j}{2} + \hat{\imath}\,\Re(n_j)k_0\right)d_j\right);$$

the propagating factor, P_j, represents accumulated phase retardation and wave attenuation in the j^{th} layer with the thickness d_j.

The MNHM structure can be considered as a five-stacked structure of a homogeneous layer (Fig. S3c). S^{15} was calculated to get the total reflection coefficient of the MNHM structure. Assuming the bottom metal reflector as a perfect mirror, a series of Redheffer star products is simplified as the following equation

$$(S^{12} * S^{23}) * (S^{34} * S^{45}) = S^{13} * S^{35} = S^{13} * \begin{bmatrix} 0 & -1 \\ -1 & 0 \end{bmatrix} = S^{15}. \quad \text{(S3-5)}$$

In detail, the reflection coefficient of the MNHM structure, r_{15}, can be rearranged as the following equation

$$r_{15} = r_{12} + \frac{t_{12}t_{21}P_2^2}{1 - r_{21}r_{23}P_2^2}\left(r_{23} + t_{23}t_{32}P_3^2\left(1 - P_3^2\left(r_{32} + \frac{r_{21}t_{32}t_{23}P_2^2}{1 - r_{21}r_{23}P_2^2}\right)\right)^{-1}\right). \quad \text{(S3-6)}$$

Finally, the total reflection is obtained as the square of the reflection coefficient (Eq. S3-7).

$$R_{15} = |r_{15}|^2 \quad \text{(S3-7)}$$

Supplementary Note 1: Schematic of the fabrication process of the proposed MNHM structure

The devices presented in the paper were fabricated through the process shown in Fig. S4. A more detailed condition can be found in the Methods.

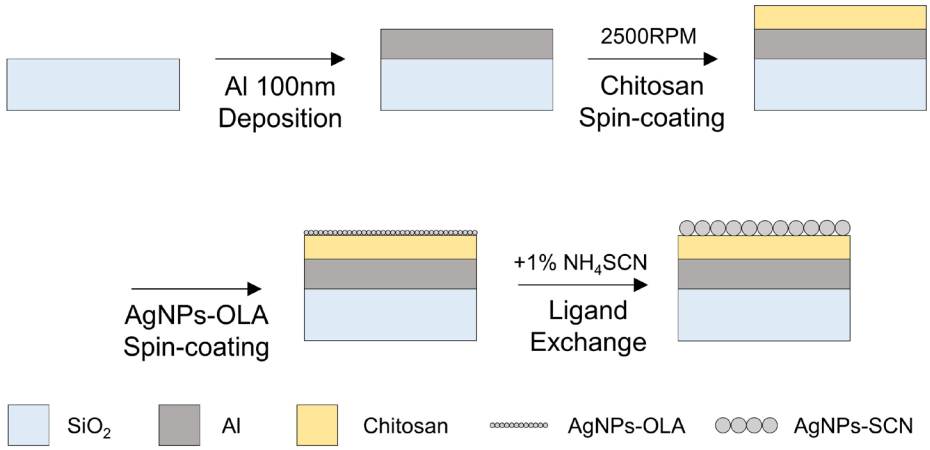

Figure. S4. The fabrication process and detailed conditions of the proposed MNHM structure.

Supplementary Note 2: Surface morphology of AgNPs-SCN layer

The surface analysis was conducted using the AFM to understand the structural characteristics of AgNPs-SCN. The measurement was carried out in contact mode with the SCN nanoparticle layer fabricated under the same conditions as in the main text. The peaks shown in Fig. S5 indicate the locations of the nanoparticles, which is consistent with the SEM images. The surface morphology data were used to obtain geometrical factors required for simulation modeling.

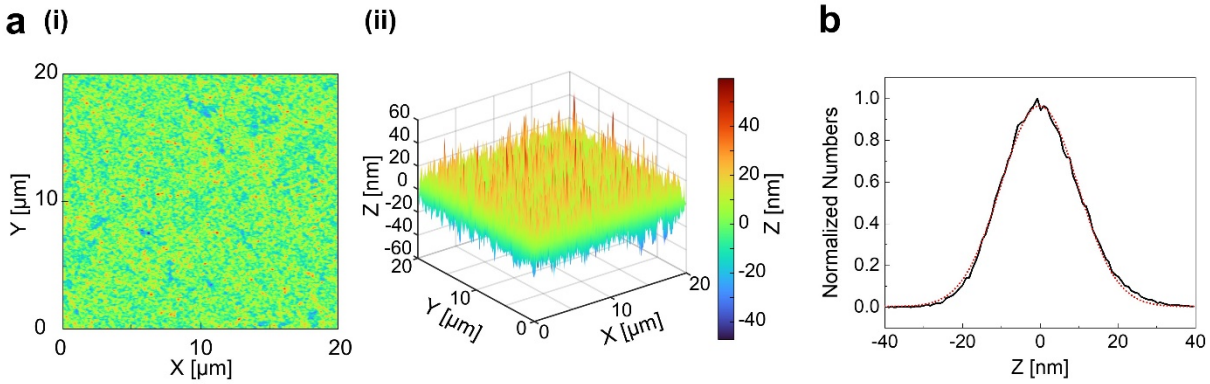

Figure S5. Structural characteristics of AgNPs-SCN layer fabricated through ligand exchange. (a) (i) topview (ii) 3D view (b) distribution of z-direction components. All data were measured using AFM.

Supplementary Note 3: Change of refractive index of the chitosan layer according to the relative humidity

The chitosan layer quickly and sensitively swells in response to ambient relative humidity. In the swelling state, the chitosan layer absorbs the surrounding moisture, and the refractive index of the chitosan layer decreases. The refractive index of the chitosan layer was measured by ellipsometry and fitted as like previous research *(46)*. This decrease in the refractive index of the hydrogel weakens the red-shift of the resonant wavelength when the chitosan is swollen *(23)*.

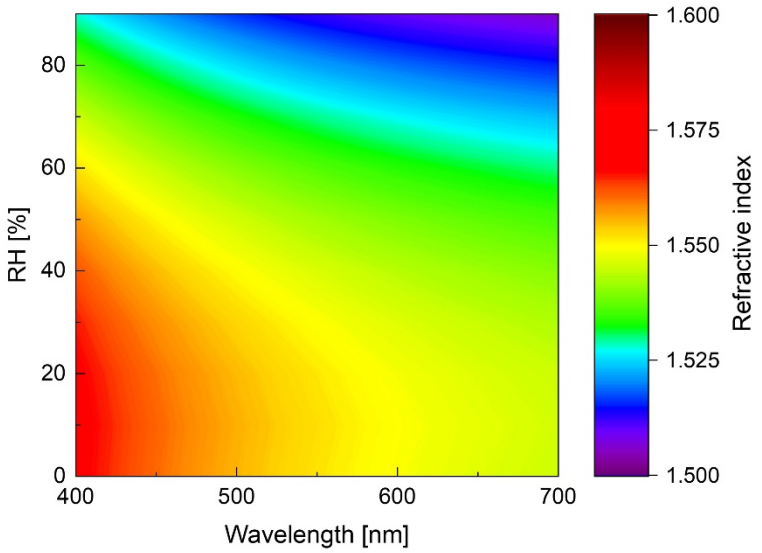

Figure S6. The change of refractive index of chitosan layer according to relative humidity.

Supplementary Note 4: Thickness of chitosan layer according to spin-coating speed

The thickness of the insulating layer can be controlled by the concentration of the chitosan solution and the spin-coating speed. Fig. S7 shows the thickness of the chitosan layer according to the concentration and the spin-coating speed in an RH 20%. All data were measured using AFM.

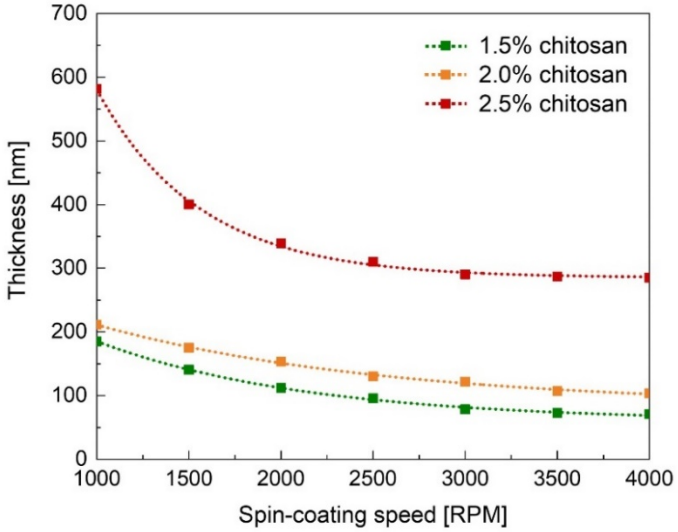

Figure S7. The thickness of the chitosan layer according to the concentration of the solution and spin-coating speed.

Supplementary Note 5: Optical system for measuring optical response according to the change of relative humidity

A special humidity chamber is designed to precisely measure the optical response of the MNHM device. This chamber is designed to check and manipulate the inside humidity in real-time. The following optical setup was used to simultaneously measure the optical image and reflection spectrum.

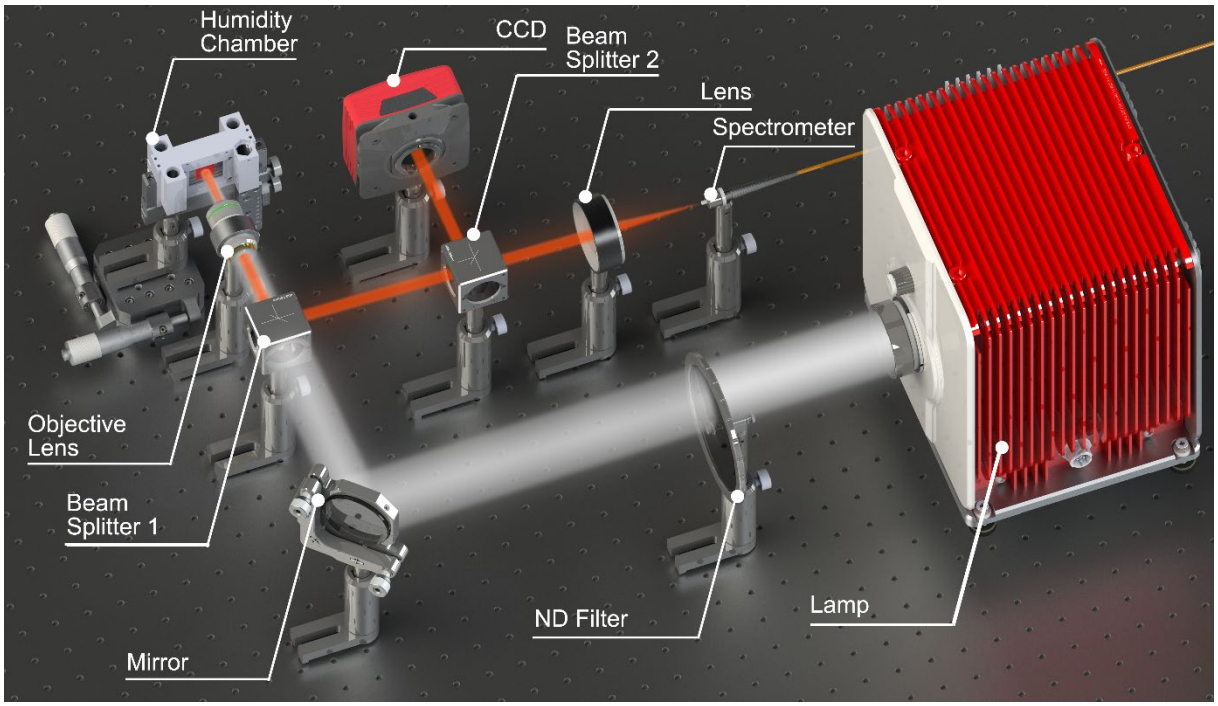

Figure S8. An optical setup for measuring the optical spectra and imaging the sensor with the change of relative humidity.

Supplementary Note 6: Influence of incident angle on the reflectance of the MNHM-SCN

Changes in the reflectance spectrum with the incident angle from 0° to 30° of the MNHM-SCN were calculated in both RH 40% and RH 90% under the TM and TE mode. In the both modes, it was observed that the peak blue-shifted as the incident angle increased (Fig. S9).

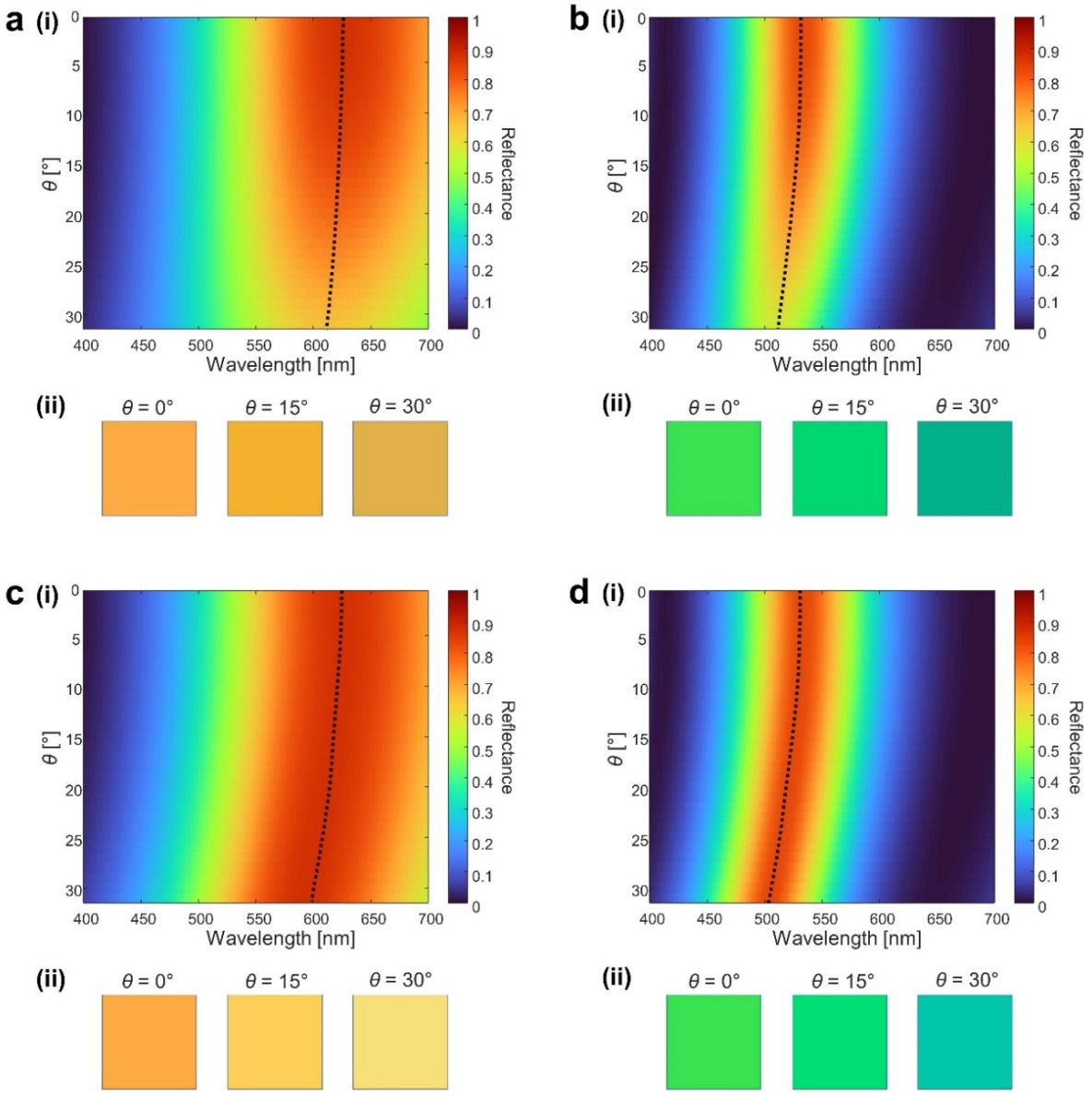

Figure S9. The change of (i) reflectance and (ii) color of MNHM-SCN etalon according to the incident angle under the TM/TE mode. (a) RH 40%, TM mode. (b) RH 90%, TM mode. (a) RH 40%, TE mode. (b) RH 90%, TE mode. The black dotted line represents the peak shift in reflectance.

Supplementary Note 7: Electrical field distribution in the effective MNHM-SCN

To support the analysis of electric field distribution in the main text, the electrical field distribution of the effective MNHM-SCN is calculated through FDTD simulation (Fig. S10). The refractive index of the effective nanoparticles is calculated through the S-parameter retrieval method mentioned in Supplementary Text 2. At the peak of the reflectance (Fig. S10a), it can be seen that the electrical field distribution inside the hydrogel layer forms a mode similar to that of Fabry-Perot resonance. The localized field in the lossy effective nanoparticle layer is weak. In contrast, a strong field is concentrated in the effective nanoparticle layer and creates a large loss at the dip of the reflectance (Fig. S10b). These field distribution data are consistent with the analysis in the main text.

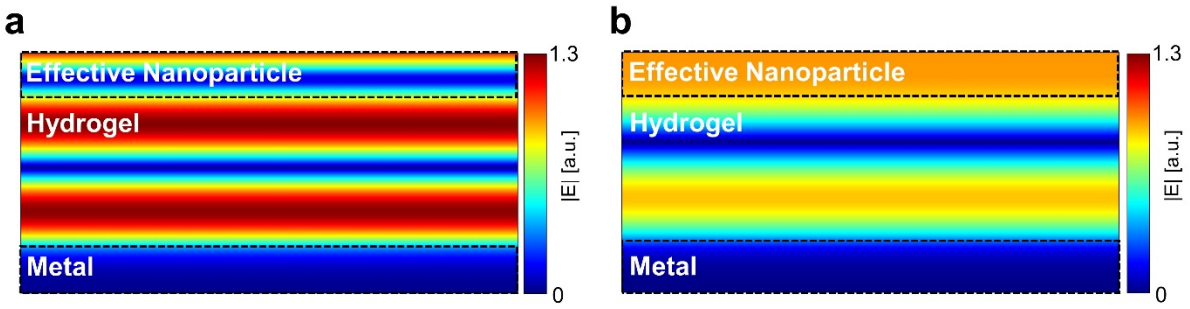

Figure S10. Electrical field distribution of effective MNHM-SCN at RH 90%. (a) at the peak of the reflectance, 532 nm. (b) at the dip of the reflectance, 676 nm.

Supplementary Note 8: Phase distribution in the near-field area of MNHM-SCN

In the MNHM-SCN (at RH 90%), the phase distribution of the reflected electrical field is numerically calculated through FDTD simulation (Fig. S11). Nanoparticles that are much smaller than the wavelength of the incident light (532 nm) reflect light similar to a plane wave. This shows that the nanoparticle layer can be well approximated as an effective layer.

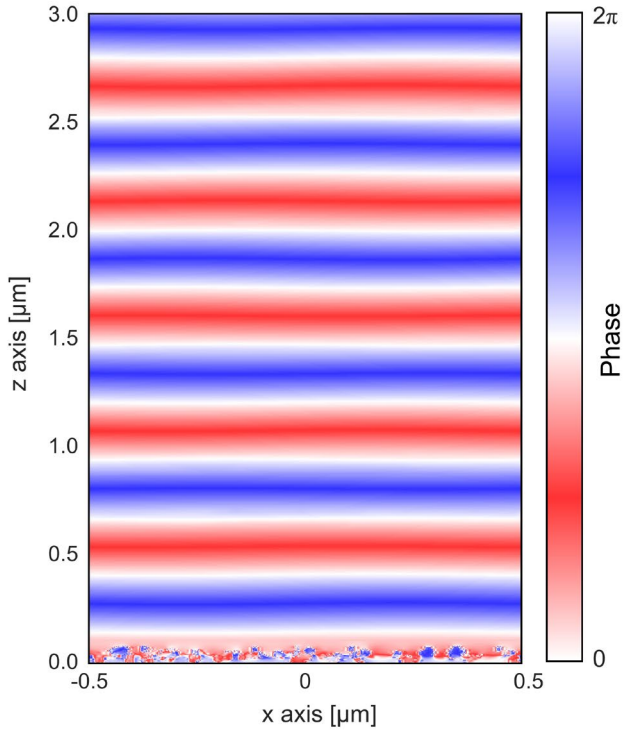

Figure S11. Phase distribution of the reflected electrical field at a MNHM-SCN.

Supplementary Note 9: Thermal stability of AgNPs layer

The stability of the device under harsh conditions such as high humidity and temperature is important for practical application. Therefore, the stability of the AgNPs-OLA and -SCN layer was examined through XRD and transmission spectra measurement under RH 85% condition. Fig. S12a displays the XRD patterns of AgNPs. Despite the high humidity conditions, oxidation such as AgO and Ag_2O was not observed in each layer. The XRD patterns and sample images show that, unlike Ag NPs-OLA, which exhibits a gradual change with increasing temperature, AgNPs-SCN has good thermal stability up to 85°C in a high humidity environment. In Fig. S12b, the transmission of AgNPs-OLA is changed as the NPs are aggregated by thermal annealing, and the transmittance is significantly lowered at 85°C. On the contrary, AgNPs-SCN layer, mainly used in this paper, showed optical property stability despite the high temperature and high humidity environment. It is considered that the oxidation reaction of Ag was retarded by the ligand surrounding the surface of AgNPs. This shows that the MNHM-SCN device can be used in harsh environments.

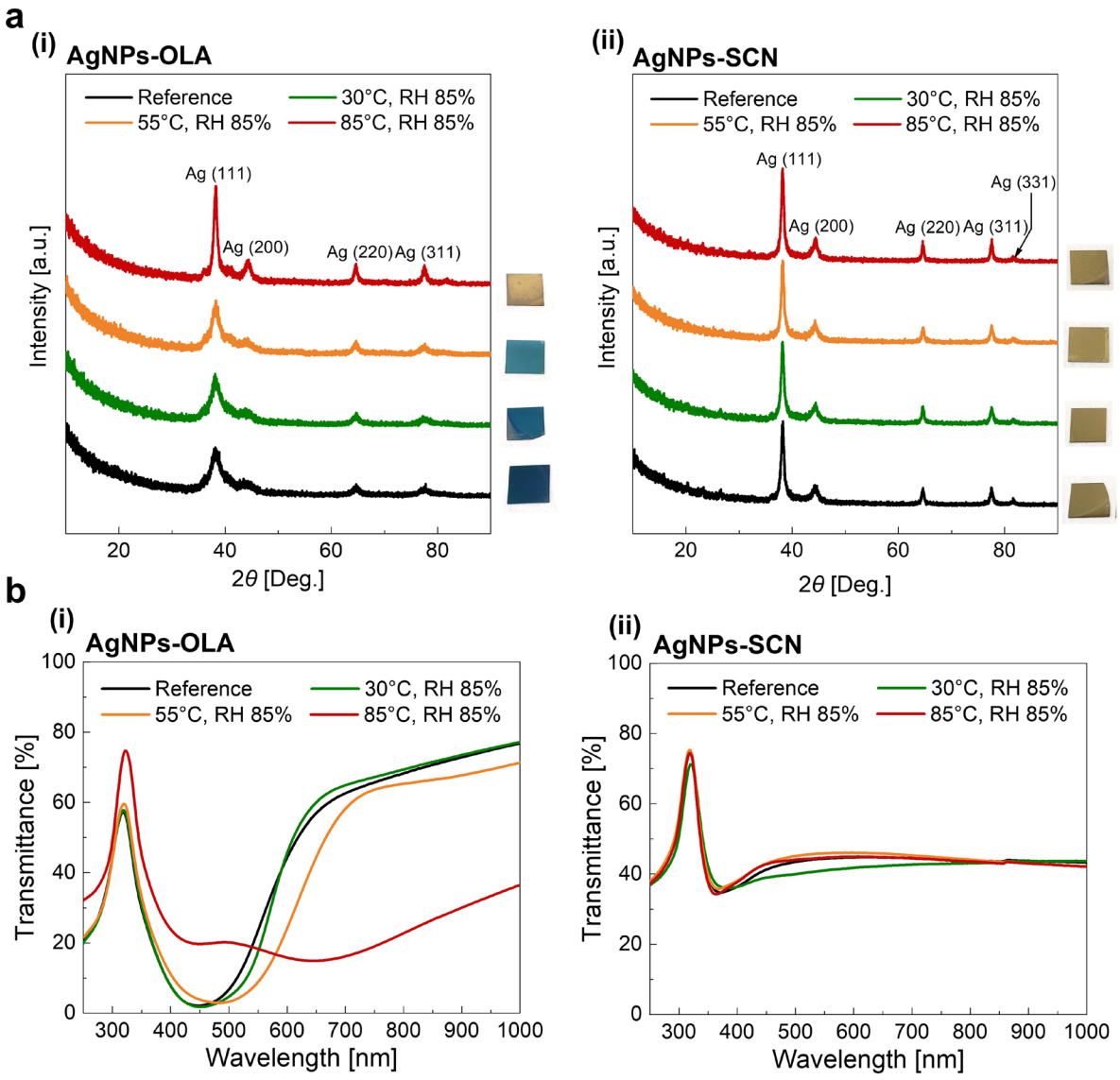

Figure S12. Thermal stability of the fabricated AgNPs-OLA and -SCN layer under high humidity conditions (RH 85%). (a) XRD patterns according to the temperature change (30°C, 55°C, and 85°C). (i) AgNPs-OLA (ii) AgNPs-SCN. (b) transmittance spectrum according to the temperature change (30°C, 55°C, and 85°C). (i) AgNPs-OLA (ii) AgNPs-SCN. Reference data were taken at 25°C, RH 20%.

Supplementary Note 10: CIE 1931 diagram of high-resolution display

The high-resolution MNHM display consists of 5 types of pixels with different heights of SiO_2 layers. The exact heights of SiO_2 layers were obtained through measurements; t_{SiO2} = 30 nm, 85 nm, 140 nm, 185 nm, 235 nm. Each pixel shows orange, red, blue, green, and yellow at RH 0%. Since this display is sensitive to humidity, we marked the color change according to the humidity change in the CIE 1931 diagram.

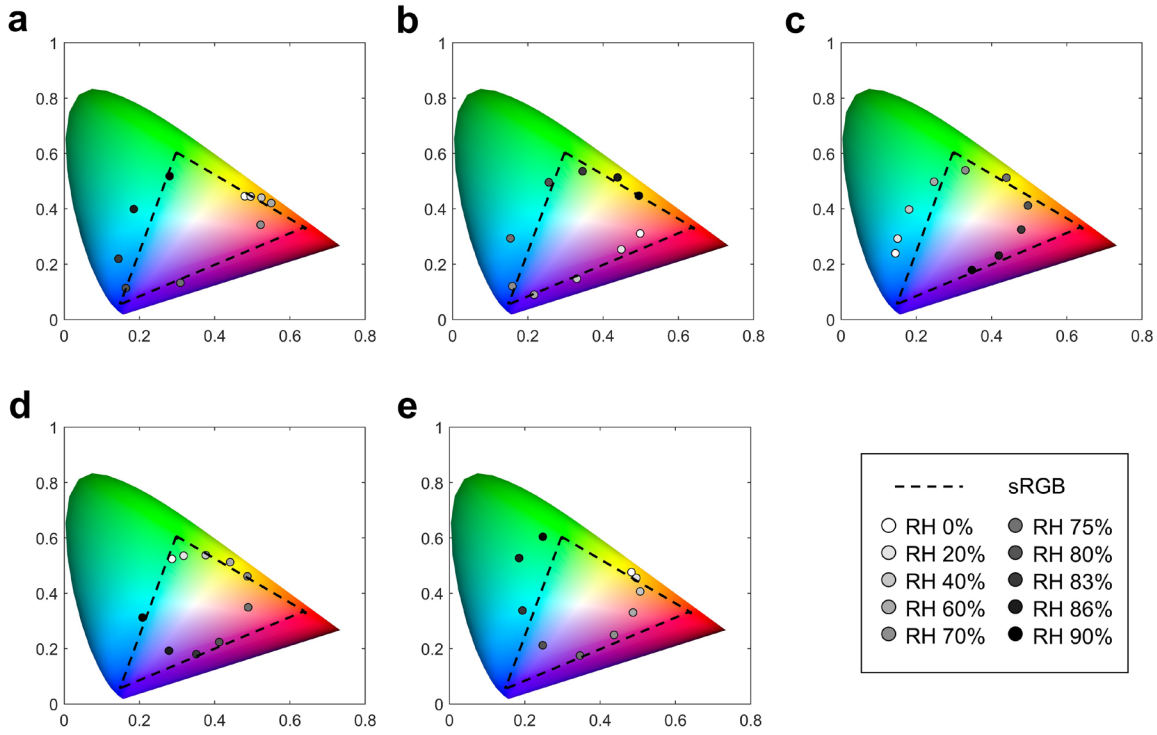

Figure S13. CIE 1931 diagram of the high-resolution MNHM display according to the RH. (a) t_{SiO2} = 30 nm. (b) t_{SiO2} = 85 nm. (c) t_{SiO2} = 140 nm. (d) t_{SiO2} = 185 nm. (e) t_{SiO2} = 235 nm.

REFERENCES AND NOTES

1. C. Wang, L. Yin, L. Zhang, D. Xiang, R. Gao, Metal oxide gas sensors: Sensitivity and influencing factors. *Sensors* **10**, 2088–2106 (2010).

2. P. Gründler, *Chemical Sensors: An Introduction for Scientists and Engineers* (Springer Berlin Heidelberg, 2007); http://link.springer.com/10.1007/978-3-540-45743-5.

3. X. Liu, S. Cheng, H. Liu, S. Hu, D. Zhang, H. Ning, A survey on gas sensing technology. *Sensors* **12**, 9635–9665 (2012).

4. M. Khan, M. Rao, Q. Li, Recent advances in electrochemical sensors for detecting toxic gases: NO_2, SO_2 and H_2S. *Sensors* **19**, 905 (2019).

5. J. Hodgkinson, R. P. Tatam, Optical gas sensing: A review. *Meas. Sci. Technol.* **24**, 012004 (2013).

6. H. Megahd, P. Lova, D. Comoretto, Universal design rules for flory–Huggins polymer photonic vapor sensors. *Adv. Funct. Mater.* **31**, 2009626 (2021).

7. F. Shu, F. Yu, R. Peng, Y. Zhu, B. Xiong, R. Fan, Z. Wang, Y. Liu, M. Wang, Dynamic plasmonic color generation based on phase transition of vanadium dioxide. *Adv. Opt. Mater.* **6**, 1700939 (2018).

8. F. Neubrech, X. Duan, N. Liu, Dynamic plasmonic color generation enabled by functional materials. *Sci. Adv.* **6**, eabc2709 (2020).

9. I. Kim, M. A. Ansari, M. Q. Mehmood, W. Kim, J. Jang, M. Zubair, Y. Kim, J. Rho, Stimuli-responsive dynamic metaholographic displays with designer liquid crystal modulators. *Adv. Mater.* **32**, 2004664 (2020).

10. I. Kim, W.-S. Kim, K. Kim, M. A. Ansari, M. Q. Mehmood, T. Badloe, Y. Kim, J. Gwak, H. Lee, Y.-K. Kim, J. Rho, Holographic metasurface gas sensors for instantaneous visual alarms. *Sci. Adv.* **7**, eabe9943 (2021).

11. S. Mohd-Noor, H. Jang, K. Baek, Y. R. Pei, A. M. Alam, Y. H. Kim, I. S. Kim, J. H. Choy, J. K.

Hyun, Ultrafast humidity-responsive structural colors from disordered nanoporous titania microspheres. *J. Mater. Chem. A* **7**, 10561–10571 (2019).

12. N. Jarulertwathana, S. Mohd-Noor, J. K. Hyun, Mesoporous solid and yolk–shell titania microspheres as touchless colorimetric sensors with high responsivity and ultrashort response times. *ACS Appl. Mater. Interfaces* **13**, 44786–44796 (2021).

13. J. Fu, F. Yang, Z. Guo, The chitosan hydrogels: From structure to function. *New J. Chem.* **42**, 17162–17180 (2018).

14. H. S. Kang, S. W. Han, C. Park, S. W. Lee, H. Eoh, J. Baek, D.-G. Shin, T. H. Park, J. Huh, H. Lee, D.-E. Kim, D. Y. Ryu, E. L. Thomas, W.-G. Koh, C. Park, 3D touchless multiorder reflection structural color sensing display. *Sci. Adv.* **6**, eabb5769 (2020).

15. A. Y. Mironenko, A. A. Sergeev, A. E. Nazirov, E. B. Modin, S. S. Voznesenskiy, S. Y. Bratskaya, H2S optical waveguide gas sensors based on chitosan/Au and chitosan/Ag nanocomposites. *Sens. Actuators B* **225**, 348–353 (2016).

16. Y. J. Yoo, W. Kim, J. H. Ko, Y. J. Kim, Y. Lee, S. G. Stanciu, J. Lee, S. Kim, J. Oh, Y. M. Song, Large-area virus coated ultrathin colorimetric sensors with a highly lossy resonant promoter for enhanced chromaticity. *Adv. Sci.* **7**, 2000978 (2020).

17. S. Daqiqeh Rezaei, Z. Dong, J. Y. E. Chan, J. Trisno, R. J. H. Ng, Q. Ruan, C. W. Qiu, N. A. Mortensen, J. K. W. Yang, Nanophotonic structural colors. *ACS Photonics.* **8**, 18–33 (2021).

18. H. Eoh, Y. Jung, C. Park, C. E. Lee, T. H. Park, H. S. Kang, S. Jeon, D. Y. Ryu, J. Huh, C. Park, Photonic crystal palette of binary block copolymer blends for full visible structural color encryption. *Adv. Funct. Mater.* **32**, 2103697 (2022).

19. M. Qin, M. Sun, R. Bai, Y. Mao, X. Qian, D. Sikka, Y. Zhao, H. J. Qi, Z. Suo, X. He, Bioinspired hydrogel interferometer for adaptive coloration and chemical sensing. *Adv. Mater.* **30**, 1800468 (2018).

20. S. Banisadr, A. Oyefusi, J. Chen, A versatile strategy for transparent stimuli-responsive interference

coloration. *ACS Appl. Mater. Interfaces* **11**, 7415–7422 (2019).

21. S. Chen, S. Rossi, R. Shanker, G. Cincotti, S. Gamage, P. Kühne, V. Stanishev, I. Engquist, M. Berggren, J. Edberg, V. Darakchieva, M. P. Jonsson, Tunable structural color images by UV-patterned conducting polymer nanofilms on metal surfaces. *Adv. Mater.* **33**, 2102451 (2021).

22. L. Yu, H. Xu, T. M. Monro, D. G. Lancaster, Y. Xie, H. Zeng, G. Y. Chen, X. Liu, Ultrafast colorimetric humidity-sensitive polyelectrolyte coating for touchless control. *Mater. Horizons.* **4**, 72–82 (2017).

23. J. Jang, K. Kang, N. Raeis-Hosseini, A. Ismukhanova, H. Jeong, C. Jung, B. Kim, J. Lee, I. Park, J. Rho, Self-powered humidity sensor using chitosan-based plasmonic metal–hydrogel–metal filters. *Adv. Opt. Mater.* **8**, 1901932 (2020).

24. H. Kwon, S. Kim, Chemically tunable, biocompatible, and cost-effective metal–insulator–metal resonators using silk protein and ultrathin silver films. *ACS Photonics.* **2**, 1675–1680 (2015).

25. S. Arif, M. Umar, S. Kim, Interacting metal–insulator–metal resonator by nanoporous silver and silk protein nanomembranes and its water-sensing application. *ACS Omega.* **4**, 9010–9016 (2019).

26. D. Chen, T. Wang, G. Song, Y. Du, J. Lv, X. Zhang, Y. Li, L. Zhang, J. Hu, Y. Fu, R. Jordan, Dynamic tunable color display based on metal–insulator–metal resonator with polymer brush insulator layer as signal transducer. *ACS Appl. Mater. Interfaces* **11**, 41668–41675 (2019).

27. S. D. Rezaei, J. Ho, A. Naderi, M. T. Yaraki, T. Wang, Z. Dong, S. Ramakrishna, J. K. W. Yang, Tunable, cost-effective, and scalable structural colors for sensing and consumer products. *Adv. Opt. Mater.* **7**, 1900735 (2019).

28. P. Mao, C. Liu, Y. Niu, Y. Qin, F. Song, M. Han, R. E. Palmer, S. A. Maier, S. Zhang, Disorder-induced material-insensitive optical response in plasmonic nanostructures: Vibrant structural colors from noble metals. *Adv. Mater.* **33**, 2007623 (2021).

29. T. Kim, E.-S. Yu, Y.-G. Bae, J. Lee, I. S. Kim, S. Chung, S.-Y. Lee, Y.-S. Ryu, Asymmetric optical camouflage: Tuneable reflective colour accompanied by the optical Janus effect. *Light Sci. Appl.* **9**,

175 (2020).

30. D. Franklin, Z. He, P. Mastranzo Ortega, A. Safaei, P. Cencillo-Abad, S.-T. Wu, D. Chanda, Self-assembled plasmonics for angle-independent structural color displays with actively addressed black states. *Proc. Natl. Acad. Sci.* **117**, 13350–13358 (2020).

31. P. Mao, C. Liu, F. Song, M. Han, S. A. Maier, S. Zhang, Manipulating disordered plasmonic systems by external cavity with transition from broadband absorption to reconfigurable reflection. *Nat. Commun.* **11**, 1538 (2020).

32. P. Mao, C. Liu, X. Li, M. Liu, Q. Chen, M. Han, S. A. Maier, E. H. Sargent, S. Zhang, Single-step-fabricated disordered metasurfaces for enhanced light extraction from LEDs. *Light Sci. Appl.* **10**, 180 (2021).

33. A. T. Fafarman, S. H. Hong, H. Caglayan, X. Ye, B. T. Diroll, T. Paik, N. Engheta, C. B. Murray, C. R. Kagan, Chemically tailored dielectric-to-metal transition for the design of metamaterials from nanoimprinted colloidal nanocrystals. *Nano Lett.* **13**, 350–357 (2013).

34. S. J. Kim, H. K. Choi, H. Lee, S. H. Hong, Solution-processable nanocrystal-based broadband fabry-perot absorber for reflective vivid color generation. *ACS Appl. Mater. Interfaces* **11**, 7280–7287 (2019).

35. D. R. Rohindra, A. V. Nand, J. R. Khurma, Swelling properties of chitosan hydrogels. *South Pacific J. Nat. Appl. Sci.* **22**, 32–35 (2004).

36. L. H. Chen, T. Li, C. C. Chan, R. Menon, P. Balamurali, M. Shaillender, B. Neu, X. M. Ang, P. Zu, W. C. Wong, K. C. Leong, Chitosan based fiber-optic Fabry–Perot humidity sensor. *Sens. Actuators B* **169**, 167–172 (2012).

37. D. Sikdar, A. A. Kornyshev, An electro-tunable Fabry–Perot interferometer based on dual mirror-on-mirror nanoplasmonic metamaterials. *Nanophotonics.* **8**, 2279–2290 (2019).

38. H.-S. Lee, M. Q. Yee, Y. Y. Eckmann, N. J. Hickok, D. M. Eckmann, R. J. Composto, Reversible swelling of chitosan and quaternary ammonium modified chitosan brush layers: Effects of pH and

counter anion size and functionality. *J. Mater. Chem.* **22**, 19605–19616 (2012).

39. D. R. Smith, D. C. Vier, T. Koschny, C. M. Soukoulis, Electromagnetic parameter retrieval from inhomogeneous metamaterials. *Phys. Rev. E Stat. Nonlinear, Soft Matter Phys.* **71**, 036617 (2005).

40. D. R. Smith, S. Schultz, P. Markoš, C. M. Soukoulis, Determination of effective permittivity and permeability of metamaterials from reflection and transmission coefficients. *Phys. Rev. B Condens. Matter Mater. Phys.* **65**, 195104 (2002).

41. L. Wang, M. S. H. Boutilier, P. R. Kidambi, D. Jang, N. G. Hadjiconstantinou, R. Karnik, Fundamental transport mechanisms, fabrication and potential applications of nanoporous atomically thin membranes. *Nat. Nanotechnol.* **12**, 509–522 (2017).

42. C. Jung, G. Kim, M. Jeong, J. Jang, Z. Dong, T. Badloe, J. K. W. Yang, J. Rho, Metasurface-driven optically variable devices. *Chem. Rev.* **121**, 13013–13050 (2021).

43. J. Li, Y. Chen, Y. Hu, H. Duan, N. Liu, Magnesium-based metasurfaces for dual-function switching between dynamic holography and dynamic color display. *ACS Nano* **14**, 7892–7898 (2020).

44. J. Li, S. Kamin, G. Zheng, F. Neubrech, S. Zhang, N. Liu, Addressable metasurfaces for dynamic holography and optical information encryption. *Sci. Adv.* **4**, eaar6768 (2018).

45. Z. Wang, C. Dai, J. Zhang, D. Wang, Y. Shi, X. Wang, G. Zheng, X. Zhang, Z. Li, Real-time tunable nanoprinting-multiplexing with simultaneous meta-holography displays by stepwise nanocavities. *Adv. Funct. Mater.* **2021**, 2110022 (2021).

46. S. S. Voznesenskiy, A. A. Sergeev, A. Y. Mironenko, S. Y. Bratskaya, Y. N. Kulchin, Integrated-optical sensors based on chitosan waveguide films for relative humidity measurements. *Sens. Actuators B* **188**, 482–487 (2013).